



Simulation and analysis of the local atomic structure for melting behavior in metals



Xinwei Wang, Mengxin Yang, Bohan Cao, Xiaoqian Gai, Yibo Sun, Fubo Tian^{*}, Liang Li^{**}

State Key Laboratory of Superhard Materials, College of Physics, Jilin University, Changchun, 130012, People's Republic of China

ARTICLE INFO

Keywords:

Melting behavior
Atomic structure
Crystal defects
Nucleation processes
Molecular dynamics simulations

ABSTRACT

Melting is a phase transition from topological order to disorder, leading a solid to transform into a liquid state. However, the microstructural principles governing the melting behavior of metals, particularly during the melting process, remain unclear. This study adopts molecular dynamics simulations to investigate the atomic structure during the melting process of metals, taking Cu as an example. The effects of crystal orientations, surfaces, and surface energies on the anisotropy of the melting point are discussed. Furthermore, the similarities and differences are described between pre-melting, surface melting, and bulk melting in Cu. The investigation addresses superheating issues arising from the inhomogeneous nucleation of crystal defects and the homogeneous nucleation of perfect crystals. Finally, a detailed exploration of the transition in the local atomic structure and the dynamic behavior of Cu atoms is conducted, utilizing the mean square displacement, diffusion coefficient, radial distribution function, and polyhedral template matching.

1. Introduction

Melting is a phase transition from a solid to a liquid, and high-pressure melting serves as a foundation for investigating the physical properties of materials [1–5]. It holds profound implications for constructing high-pressure equations of state in materials [1,6–8] and provides insights into the structure and variation of the solid and liquid phases of materials at critical conditions [9–11]. However, the microstructural principles associated with the melting behavior of materials remain unclear during the melting processes, leading to considerable controversy and disagreement between experimental techniques and numerical simulation studies of melting [9,12,13]. Researchers have proposed corresponding theoretical criteria for melting based on lattice instability models [14–17], including Lindemann melting, mechanical instability, thermoelastic instability, and defect melting criteria. These empirical theories consider melting as a process of bulk melting caused by lattice elastic instability or defects with increasing temperature, resulting in a bulk melting point (T_m) above the thermodynamic T_m .

The experiments indicate that the melting processes of crystals originate from the inhomogeneous nucleation of the liquid within the crystal surface or internal interface [18], and not bulk melting from the inside out. Namely, the appearance and quantity of a crystal surface or

internal interface determine the thermodynamic melting and its procedure [18–20]. Since the surface atoms in a highly asymmetric state, are placed in a different environment than the internal atoms, the suspended bond appears on the side of the non-periodic boundary due to the lack of nearest neighbor atoms. The arrangement of atoms on the surface must be distorted from an energy perspective, thus reducing the number of suspended bonds to achieve the lowest energy stability. Consequently, the arrangement of surface atoms differs significantly from the internal atoms, and the melting of materials can be divided into two types. One type is homogeneous nucleation melting [21–23], where the liquid grows nucleated in the solid, and melting may occur everywhere. Another type of melting is inhomogeneous nucleation [9,18,21,24,25], where melting is more likely to occur from the surfaces and defects. Inhomogeneous nucleation melting is classified into surface melting, interface melting, and melting at dislocations, vacancies and other weaker defects [9,18,21,24,25]. Surface melting is restrained due to the imposed periodic boundary conditions, which are significant theoretically but difficult to achieve experimentally. Homogeneous nucleation melting occurs together with inevitable superheating [9]. In the case of inhomogeneous nucleation melting, atoms at the surface or defects generally have higher free energy than those inside a perfect crystal. Melting can proceed even below T_m with sufficiently high free

* Corresponding author.

** Corresponding author.

E-mail addresses: tianfb@jlu.edu.cn (F. Tian), liliang@jlu.edu.cn (L. Li).

energy, known as pre-melting [18,26]. Otherwise, the material is heated significantly above its bulk T_m and metastable crystals are formed.

Recently, Fan et al. [18,26–28] demonstrated that diffusive atoms do not move randomly; instead, they move together in a highly synchronized way to form chains and even rings of atoms. The number of these extended atomic structures increases further as the temperature rises to T_m . Melting occurs when these highly correlated structures diffuse, representing a new atomic mechanism radically different from the atomic motion under the Lindemann law [29,30]. The atoms within the crystal are not only involved in vibrations but also in other types of atomic motion during the heating process. These motions contribute significantly to the total atomic displacements, mainly in the form of thermal vibrations at temperatures far below T_m . In contrast, diffusion starts at relatively high temperatures [28], directly affecting the existence state of a melting system. It is interesting to explore in-depth the factors that affect the crystal during heating and melting [9,31]. For this purpose, the effects of homogeneous nucleation, inhomogeneous nucleation, crystal orientation, surface, and structural transitions during melting on the melting behavior have been investigated using molecular dynamics (MD) simulations. The dynamics behavior of the atoms is also explored using atomic analysis techniques.

2. Simulation methods

2.1. Molecular dynamics simulations

The LAMMPS package [32] is utilized to construct the initial configuration of Cu atoms and calculate its T_m and other related properties during MD simulations. The experimental lattice constant of Cu is 3.615 Å [33], with x , y , and z corresponding to [100], [010], and [001] orientations, respectively. To eliminate the influence of surfaces and defects, the periodic boundary conditions are applied in the x , y , and z directions, and other simulation conditions align with the Ref. [21]. The simulation is conducted with a time step of 1 fs, and data on temperature, energy, volume, and atom position are generated. For simulations with surfaces of (100), (110), and (111), a cuboid system of $12a \times 12a \times 18a$ and a heating rate of 1×10^{12} K/s are selected. For simulations with crystal orientations of [100], [110], and [111], the conditions are $16a \times 16a \times 16a$ at 1×10^{12} K/s, and $30a \times 30a \times 30a$ at 1×10^{11} K/s. For the simulation with crystal defects, the system of $14a \times 14a \times 14a$ is selected, removing the atomic number of $4a \times 4a \times 4a$. For the simulation regarding the dynamic behavior of atoms, the conditions are $16a \times 16a \times 16a$ at 1×10^{12} K/s. In the simulation of the surface, the periodic boundary conditions are used in the x and y directions, and free boundary conditions are used in the z direction. The remaining stages are simulated with the periodic boundary conditions in the x , y , and z directions, and the simulation time for each stage is 1.8 ns, using the NPT ensemble, respectively. The interaction among the Cu atoms described by the Embedded Atom Method (EAM) proposed by Mishin et al. [33]. The total potential energy of the crystal within the EAM potentials can be expressed as

$$U(r_{ij}) = \sum_i F_i(\rho_i) + \frac{1}{2} \sum_{j \neq i} \varphi_{ij}(r_{ij}), \quad (1)$$

where the F_i is the embedding energy and the second term is the pair potentials. ρ_i is the sum of the electron cloud densities produced at the i th atom by the out-of-nuclear electrons of all but the i th atom, which can be expressed as

$$\rho_i = \sum_{j \neq i} f_j(r_{ij}), \quad (2)$$

where f_j (r_{ij}) is the charge density contributed by the out-of-nuclear electrons of the j th atom at the i th, and r_{ij} is the distance between the i th atom and the j th.

2.2. Atomic analysis techniques

2.2.1. Radial distribution function

The radial distribution function (RDF) is an effective method for characterizing the structural features of liquids and solids [9,13]. The RDF peak of the crystal is sharp and evident at room temperature. In the liquid state, part of the RDF peak disappears and the remaining part exhibits a diffuse peak. The RDF is defined by

$$\text{RDF} = \frac{V}{N^2} \left\langle \sum_{i=1}^{N_i} \frac{n_i(r)}{4\pi r^2 \delta r} \right\rangle, \quad (3)$$

where V and N represent the volume and number of atoms respectively, N_i represents the number of atoms around the i th atom, $n_i(r)$ represents the number of atoms found in a spherical shell around the i th atom within a distance of r to $r + \delta r$.

2.2.2. Mean square displacement

The mean square displacement (MSD) [9,13] of the system generally vibrates around the maximum value with time for solids and appears to universally increase with time for liquids. The MSD is defined as:

$$\text{MSD} = \frac{1}{N} \left\langle \sum_{i=1}^N |r_i(t) - r_i(t_0)|^2 \right\rangle, \quad (4)$$

where $r_i(t)$ represents the position of atom i at time t , t_0 is the arbitrary time origin, and $\langle \rangle$ denotes time average. According to Einstein's diffusion law, MSD enables the characterization of the diffusion behavior of metal atoms. The slope of the MSD curve is denoted as diffusion coefficient (D) for the material [9,13]:

$$D = \lim_{t \rightarrow \infty} \frac{1}{6t} \text{MSD}(t), \quad (5)$$

where t represents the correlation time, the MSD can effectively distinguish between solid and liquid states, making it a suitable tool for assessing the melting behavior of materials.

2.2.3. Polyhedral template matching

The polyhedral template matching method (PTMM) is a mathematical based on the root mean square deviation (RMSD) to assess the structural similarity between two points [34]. For any two given atoms, its RMSD can be defined as:

$$\text{RMSD}(\mathbf{A}, \mathbf{B}) = \sqrt{\frac{1}{N} \sum_{i=1}^N \| \mathbf{A}_i - \mathbf{B}_i \|^2}. \quad (6)$$

For the superposition of more than two polyatomic systems, the primary task is to identify a rotation vector \mathbf{A} and a scaling vector \mathbf{B} to minimize RMSD. Then the structural similarity between the standard cluster templates, such as simple cubic (SC), body-centered-cubic (BCC), hexagonal-closed-packed (HCP), face-centered-cubic (FCC), and icosahedral (ICO) structures, and the target cluster configuration is assessed based on RMSD.

3. Results and discussion

3.1. The effect of surface on melting behavior

To address the complexity arising from extensively variable defects and to reveal the common physical properties underlying melting, a periodic boundary condition is applied to simulate the melting of perfect crystals. Consequently, significant superheating occurs [9,21], while the actual arrangement of surface atoms undergoes relaxation, reconfiguration, adsorption, and the formation of compounds. Meanwhile, both experiments and simulations illustrate the dominance of the surface or inner interface during the melting processes [18,19,21]. The surfaces for

(100), (110), and (111) are discussed to further explore the pre-melting phenomenon, comprising 10656, 21024, and 42240 atoms, respectively, where the periodic boundary conditions are applied in the x and y directions, and free boundary conditions in the z direction. Fig. 1(a)–(h) provides the evolution of the atomic structure along the (100) surface as the melting occurs for a cuboid system of $12a \times 12a \times 18a$ at a heating rate of 1×10^{12} K/s. Free boundary conditions are adopted during the simulation, as a specific number of atoms are located on the model surface. The surface atoms exhibit fewer coordinating atoms than those inside the system, resulting in higher energies for the surface atoms, as depicted in Fig. 1(a) for the top and bottom layers of surface atoms at 0.0 ns. The atomic pairs' spacing formed between these surface atoms and the near surface atoms is also larger than that inside the system, subjecting some surface atoms to a tensile state [26]. The additional energy, provided by the high temperature, alters the distance between surface atoms as the temperature increases. When the atomic spacing exceeds the elastic limit for inter-atomic interactions, atoms change position, leading to structural rearrangement of the atoms on the system's surface. The impact on the melting behavior of the atoms begins to manifest as pre-melting [18,26], introducing significant distinctions in the structural transitions of the atomic stacks inside the system and their corresponding structural transition temperatures. According to Fig. 1 (a)–(h), the surface atoms have fewer nearest neighbors and weaker bonds. The high temperature provides surface atoms with additional energy, enabling them to overcome lattice barriers and escape lattice constraints. Above T_m , the surface atoms lose their long-range correlations, leading to the disordering of surface atoms and pre-melting. Gradually, they move inward until the system is completely melted. Fan et al. [18,26–28] proposed a mechanism distinct from Lindemann melting, suggesting that melting occurs due to the formation of chains or clusters in atoms. According to the energy–temperature (E – T) relationships, melting of the (110) and (100) surfaces occur at temperatures of 1347 K and 1378 K, respectively, in good agreement with the result of 1364 K [18]. Fig. 1(h) shows the complete melting of the (100) surface at 1420 K, which contradicts the E – T curves for $T_m = 1378$ K. The reason

for this discrepancy is that the energy and volume of the system experience a sudden change when the majority of atoms become disordered, and this corresponding temperature is considered to be T_m . The surface T_m of the (111) is 1445 K, exceeding the experimental result of 1357 K [35] but significantly below the result of 1620 K for a perfect crystal system of $12a \times 12a \times 18a$. The results reveal remarkable anisotropic behavior in the melting of the three surfaces, with the order of surface T_m being (111) > (100) > (110). The T_m obtained for the three surfaces is considerably lower than the T_m for bulk melting. Bulk melting is a homogeneous nucleation process, indicating that melting occurs with equal probability throughout the system, causing the atoms to heat up to a higher temperature before melting begins.

In addition, the surface energies of the (100), (110), and (111) are calculated from the equations $\gamma = \frac{E_{\text{final}} - E_0}{2A}$, where E_0 and E_{final} represent the energy before and after separation respectively, and A represents the surface area. The surface energies obtained are $\gamma(100) = 1344$ mJ/m², $\gamma(110) = 1470$ mJ/m², $\gamma(111) = 1251$ mJ/m² and are consistent with existing results [36,37]. The order is $\gamma(110) > \gamma(100) > \gamma(111)$, in contrast to the T_m , where the higher the surface energy, the lower the temperature the melting occurs [26]. The magnitude of the surface energy depends on the arrangement of the surface atoms. The closer the surface atoms are arranged, the stronger the inter-atomic interactions and thus the lower the surface energy of the material. Therefore, the atom-dense arrangement of surfaces has the smallest energy. The (111) surface has the highest atomic density and the most probable free external surface is the (111) for Cu.

For the cuboid model in our study, the only free surface is along the z direction, which limits the surface area of the material to some extent. To increase the contact area between the surface and the vacuum, we adopt a sphere model for further discussions on surface melting. The sphere model, with a radius of $10a$ and a heating rate of 1×10^{12} K/s, is selected, along with a vacuum layer of $2a$. The simulation employs the periodic boundary conditions and the vacuum layer, resulting in the formation of the free surface of materials. As shown in the section in Fig. 2(a)–(h), the bonds of the atoms on the surface break as the crystal

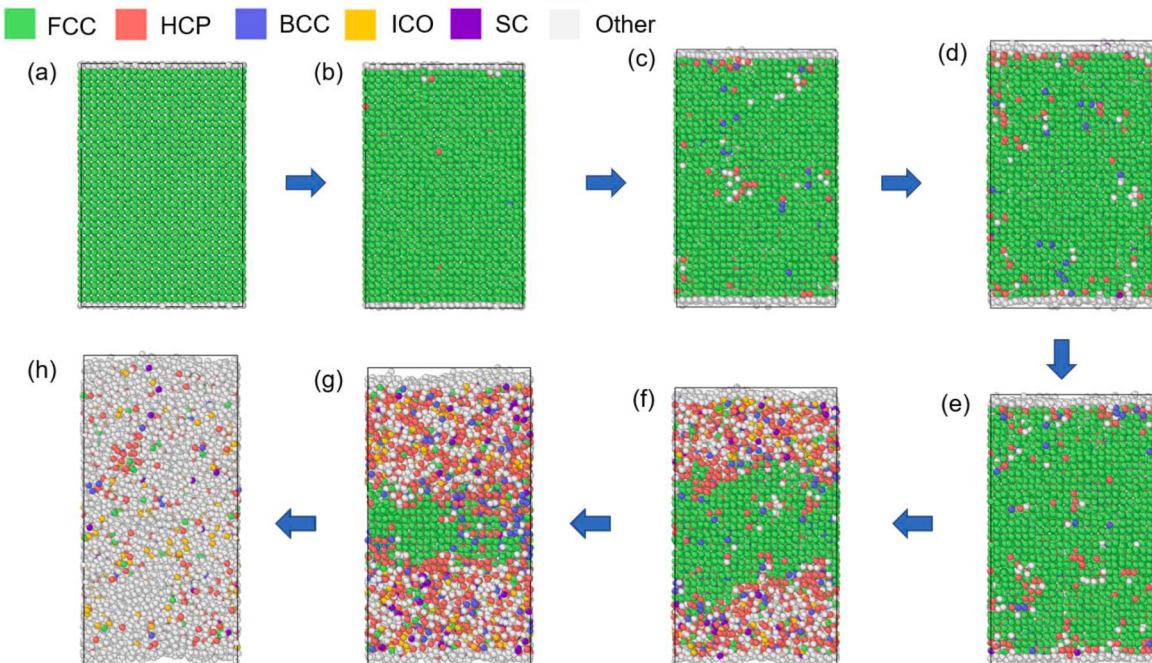


Fig. 1. Simulation of the atomic structure along the (100) surface for the system of $12a \times 12a \times 18a$ at a heating rate of 1×10^{12} K/s. The x , y , and z directions correspond to the [100], [010], and [001], with a periodic boundary condition in the x and y and free boundary condition in the z direction. The simulation times are (a) 0.0 ns at 300 K, (b) 0.7 ns at 1000 K, (c) 0.95 ns at 1250 K, (d) 1.01 ns at 1310 K, (e) 1.06 ns at 1360 K, (f) 1.1 ns at 1400 K, (g) 1.11 ns at 1410 K, and (h) 1.12 ns at 1420 K, respectively. The diagram represents the FCC in green, the HCP in red, the BCC in blue, the SC in purple, the ICO in yellow, and the Other clusters in white.

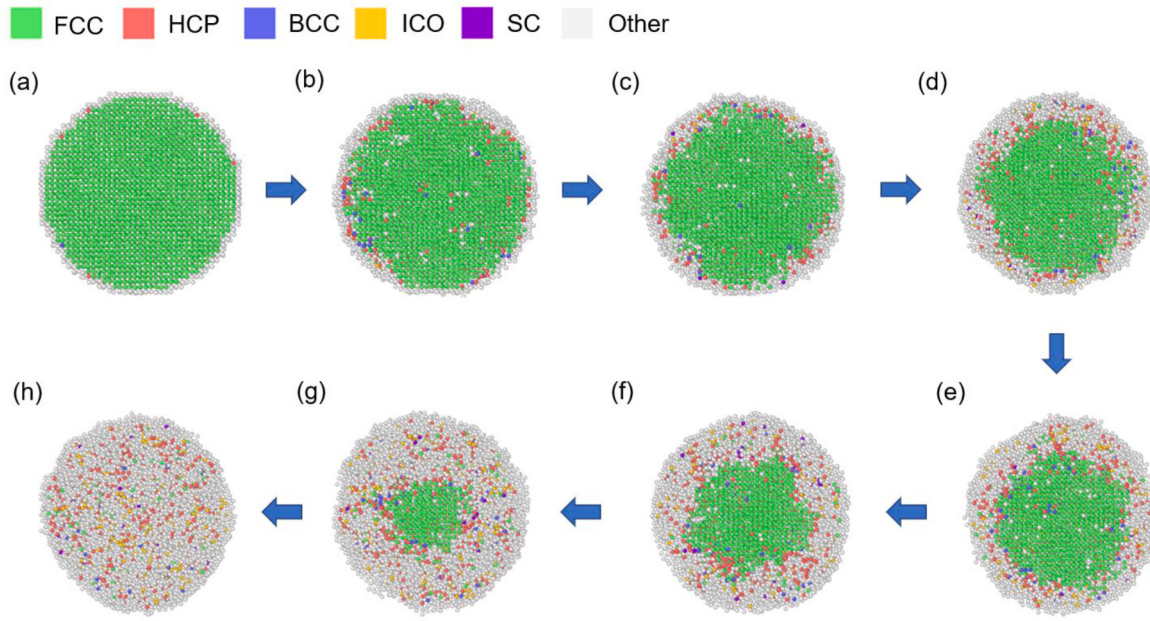


Fig. 2. In the sphere model, the system is $r = 10a$ and the heating rate is 1×10^{12} K/s. The simulated times are (a) 0.53 ns at 830 K, (b) 0.94 ns at 1240 K, (c) 0.96 ns at 1260 K, (d) 0.98 ns at 1280 K, (e) 0.99 ns at 1290 K, (f) 1.0 ns at 1300 K, (g) 1.01 ns at 1310 K, and (h) 1.02 ns at 1320 K, respectively.

forms a surface, distinct from the atoms inside the crystal. The surface atoms are only partially combined with other atoms and have fewer neighboring atoms than inside the crystal, forming the surface with higher energy than the internal atoms. The overall energy is, therefore, higher than without the addition of the vacuum layer. At 830 K (Fig. 2(a)), the atoms on the surface of the sphere become disordered, while the internal atoms are arranged in an FCC structure. With the gradual increase in temperature, the additional energy provided by the high-temperature causes a large vibration in the position of these surface atoms. The rapid increase in the number of atoms melting on the surface is evident at 1300 K (Fig. 2(f)), until complete melting occurs at 1320 K (Fig. 2(h)). The surface melting of both the cuboid and the sphere is progressive from outside to inside. However, the sphere model provides a lower $T_m = 1320$ K than the cuboid model because the surface area of the sphere is larger than that of the cuboid.

3.2. The effect of orientation on melting behavior

The melting of atoms along the [100], [110], and [111] directions is explored. The evolution of atomic energy, volume, and density with temperature along the [100] direction for the $16a \times 16a \times 16a$ and a heating rate of 1×10^{12} K/s is displayed in Fig. 3. These properties change rapidly with increasing temperature at 1613 K, indicating that the system is undergoing melting, and the T_m are found to be 1617 K and 1614 K along the orientations of [110] and [111], respectively. There is a higher degree of superheating for the T_m obtained along different orientations compared to surface melting. The simulation results reveal that the T_m along the [100], [110], and [111] directions are approximately consistent and there is no significant orientation anisotropy. Furthermore, the melting processes involving homogeneous nucleation with a perfect crystal are discussed as an initial model. The atomic structure evolution along the [100] direction for the $30a \times 30a \times 30a$ system, with a heating rate of 1×10^{11} K/s is illustrated in Fig. 4(a)-(f). At 1450 K (Fig. 4(a)), numerous liquid clusters (liquid nuclei) are present in the system. In this case, the liquid nuclei are relatively small and discrete, with most of them constantly changing in size and disappearing as the temperature rises. In the simulation, certain locations experience the sudden appearance of a new liquid nucleus, and the whole system undergoes various transformations. This continues until 1591 K (Fig. 4

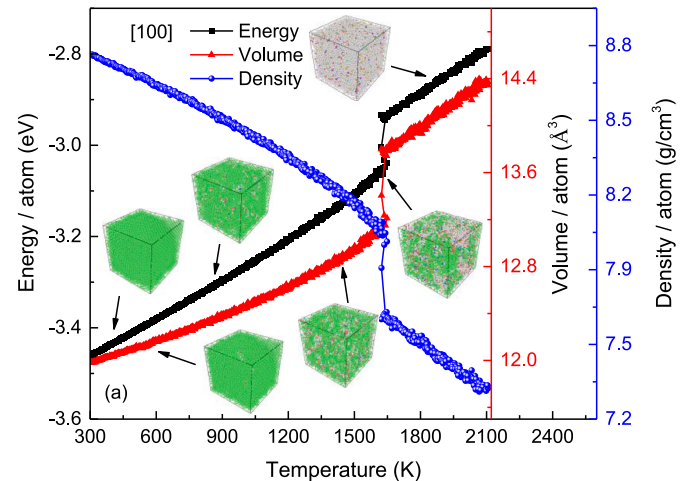


Fig. 3. Evolution of atomic energy, volume, and density with temperature along the [100] orientation for a system of $16a \times 16a \times 16a$ with a heating rate of 1×10^{12} K/s.

(c)) when the dominance of a liquid nucleus becomes evident. As the temperature rises, it no longer decreases but rather increases, while most of the other small liquid nuclei still fluctuate. The previously dominant liquid nuclei also grow larger, leading to collisions and the formation of a larger liquid clusters. They continue to grow with increasing temperatures up to 1593 K (Fig. 4(e)), when the other dominant nuclei are also connected to form a major nucleus. Growth becomes more rapid thereafter, with an increasing number of liquid nuclei appearing around each 1 K increase in temperature. The liquid atoms become increasingly numerous until all the liquid nuclei are connected, finally melting completely at 1594 K (Fig. 4(f)). The lower $T_m = 1619$ K for the $16a \times 16a \times 16a$ is applied in the simulation due to the larger system and slower heating rates. The atomic structure evolution relation in Fig. 4 obviously reveals that the melting of the perfect crystal model is still a homogeneous nucleation process. Compared to the melting process of inhomogeneous nucleation, this is the essential reason why the T_m with

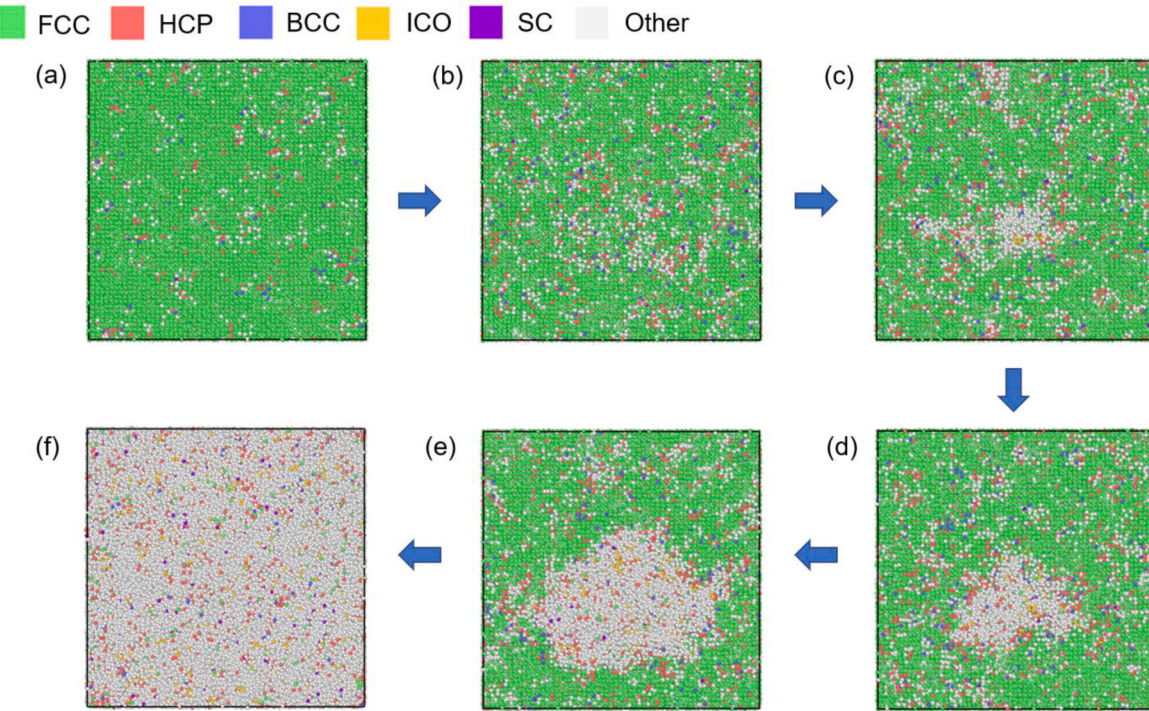


Fig. 4. Evolution of the atomic structure during melting along the [100] orientation for a system of $30a \times 30a \times 30a$ with a heating rate of 1×10^{11} K/s. The simulated time sequence includes (a) 0.0 ns at 1450 K, (b) 1.40 ns at 1590 K, (c) 1.41 ns at 1591 K, (d) 1.42 ns at 1592 K, (e) 1.43 ns at 1593 K, and (f) 1.44 ns at 1594 K, respectively.

perfect crystals as a model is above the experiment [9]. In comparison with surface melting, melting caused by different crystal orientations belongs to bulk melting, and pre-melting exists in both melting processes. However, pre-melting in the process of surface melting takes place at a lower temperature, so the final research results reveal that the temperature of surface melting is lower than that of bulk melting.

3.3. The effect of crystal defects on melting behavior

The inevitable defects in the periodic arrangement of solid atoms in the material's actual environment leads to a diverse and complex melting process, manifested concretely by superheating and pre-melting [9,18]. Melting begins with the formation of a liquid nucleus and critical

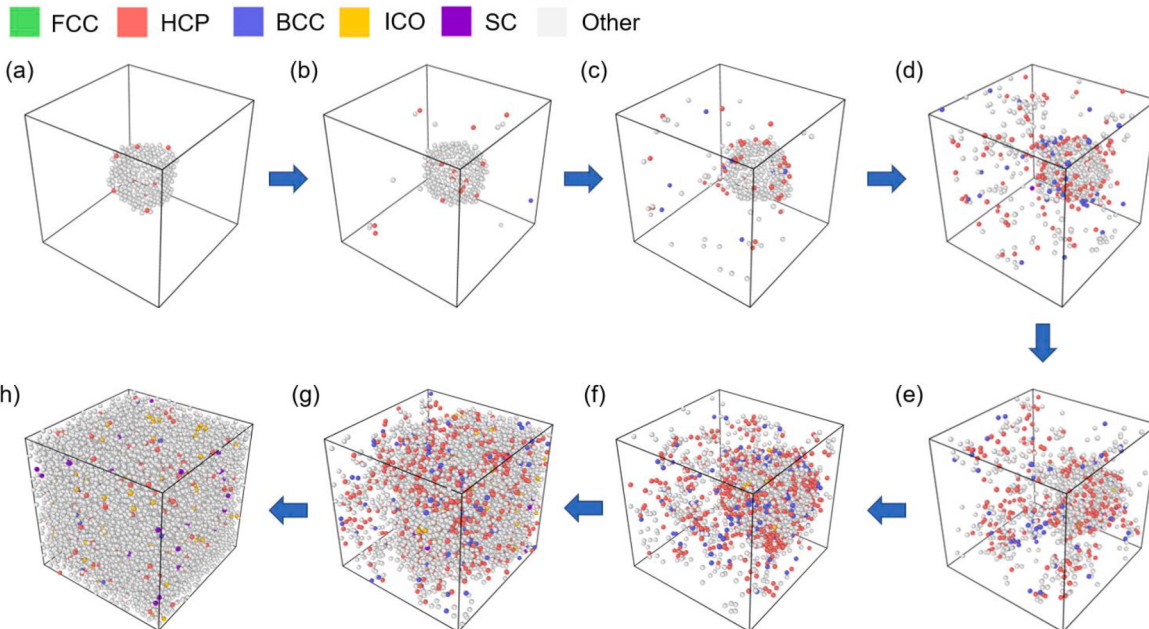


Fig. 5. Investigation of the melting process for creating of a cubic defect of $4a \times 4a \times 4a$ in the $14a \times 14a \times 14a$ system, with atomic structure evolution times of (a) 0.0 ns at 300 K, (b) 0.55 ns at 850 K, (c) 0.74 ns at 1040 K, (d) 0.88 ns at 1180 K, (e) 0.99 ns at 1290 K, (f) 1.02 ns at 1320 K, (g) 1.15 ns at 1450 K, and (h) 1.17 ns at 1470 K.

nucleus because defects, such as free surfaces, lower the free energy barrier for nucleation and strongly influence the melting process [13,18, 21,26,27]. The atomic structure variations during the melting process are illustrated in Fig. 5(a)–(d) for the $14a \times 14a \times 14a$ system with the cubic defect of $4a \times 4a \times 4a$ removed [9,13]. The defects are positioned at the center of the $14a \times 14a \times 14a$, and the atoms adjust their position by movement when the system is exposed to a lower temperature. After the structure has relaxed to equilibrium at this temperature, the atoms vibrate thermally around their equilibrium position, for instance, the atomic structure at 0.0 ns (Fig. 5(a)). As the temperature gradually increases, the atoms around the defect move at 0.74 ns (Fig. 5(c)). The defect becomes more noticeable at 0.88 ns (Fig. 5(d)), where it gradually forms the liquid nuclei [21]. The dominance of the liquid nuclei persists until 1.02 ns (Fig. 5(f)), after which they continue to grow with increasing temperature. The liquid atoms gradually envelop the solid regions until all the liquid nuclei are connected, occupying the entire system. Complete melting of the system occurs at 1.17 ns (Fig. 5(h)), consistent with the $T_m = 1465$ K from the E - T curves in Fig. 6. The reason for this can be traced to the initial defects in the model, reducing the difficulty of liquid nucleation. The existence and movement of defects enable the system to possess high energy. With increasing temperatures, the movement of defects accelerates the random motion of atoms in the system, leading to increased internal disorder of Cu atoms. The elevated energy of the system reduces the energy difference between the superheated crystal and the liquid at that temperature, allowing crystals with more defects to melt at lower temperatures [9,13, 18,21]. This phenomenon can also be explained by classical nucleation theory, where the high heating rates or movement of defects provide the motivation for the formation and growth of the liquid. Similar to the homogeneous nucleation process, the melting of inhomogeneous nucleation typically begins from crystal defects. Additionally, the existence of defects reduces the superheating of the system, and the obtained T_m is closer to reality, as depicted in Fig. 6.

3.4. The transition of atomic structure during melting

The Cu atoms exhibit FCC structures at room temperature. To investigate the transition of the atomic structure of Cu at elevated temperatures using the PTMM methods [34] in the OVITO package [38], simulations are performed at $16a \times 16a \times 16a$ and $12a \times 12a \times 12a$ with heating rates of 1×10^{12} K/s and 1×10^{13} K/s. The temperature dependence of the FCC, HCP, BCC, SC, ICO, and Other clusters in the system is illustrated in Fig. 7(a)–(d). Based on the evolution of the

atomic structure of the system with temperature, the melting processes are divided into three stages: low-temperature relaxation, rapid melting, and high-temperature equilibration [21], as shown in Fig. 7(d). Within the low-temperature relaxation, atoms continuously change position with increasing temperature, resulting in homogeneous liquid nucleation inside the system. However, the small number of the liquid nuclei has no significant effect on the energy of the system, and hence it remains a solid at the macroscopic level. In the second stage, small liquid nuclei in various positions grow as the temperature continues to rise, and more critical nuclei of the liquid appear, becoming increasingly large. The atomic structure of the system begins to change abruptly, indicating that the system has become disordered at the macroscopic level. In the third stage, the system melts completely as the liquid atoms become abundant. This stage belongs to the equilibrium period after thorough melting, when the atomic movements within the system are extremely intensive. A comparison of the atomic structures during the three stages reveals that the melting processes proceed gradually [18, 26]. During the low temperature range, the FCC tends to decrease slightly at the onset of the temperature increase from 300 K for both high and low heating rates. The FCC decreases sharply as the temperature approaches T_m , while the Other clusters increase rapidly. Simultaneously, the HCP also increases rapidly, probably due to the fact that both the FCC and HCP are the most densely packed, and they both share a density of 0.74. The FCC is distributed in a dense plane of (111) with the stacking order ABCABC, and the HCP has the same atomic distribution of atoms in a dense plane of (0001) as the BCC in the (111) plane but with the stacking order ABAB [39]. As the temperature of the system increases, the vibrational amplitude of the atoms intensifies, causing a transition from the stacking order. This is the reason why the number of HCP is substantially higher than other structures. Subsequently, the structures of BCC and SC also increase steeply at the moment of T_m . The number of Other clusters reaches a maximum above T_m , while the HCP and ICO start to decrease from their maximum values. The BCC also begins to decrease, consistent with the melting of a crystal into a liquid. Although the number of SC is low at higher temperatures, their number has not changed significantly with increasing temperature. In short, Fig. 7(a)–(d) reveal a physical law: the rapid transition of atomic structures to HCP, ICO, FCC, SC, and Other clusters in the vicinity of T_m as the FCC disappears sharply. This melting law does not change with increasing the heating rates. However, the heating rates significantly affect the melting and superheating behavior of Cu atoms. The temperature dependence of the local structure for the $16a \times 16a \times 16a$ and $12a \times 12a \times 12a$ is investigated at an equal heating rate of 1×10^{12} K/s. It can be noticed that the $T_m = 1613$ K obtained for the $16a \times 16a \times 16a$ (Fig. 7(a)) is significantly below the $T_m = 1623$ K for the $12a \times 12a \times 12a$ (Fig. 7(c)). The same result holds for a heating rate of 1×10^{13} K/s. The results illustrate that the number of atoms contained in the system does not have a significant impact on the local structure of Cu atoms before and after melting. However, the temperature remains the major factor influencing the distribution of the atomic structure, which is also in essential agreement with the T_m from the E - T and V - T curves in the previous section.

3.5. The dynamic behavior of atoms during melting

To determine whether the system is a disordered solid or a liquid immediately after melting and to assess the mobility of the atoms, an essential criterion is the MSD curves for this process, presented as a function of time [9]. The variation of the MSD and D with temperature for the $16a \times 16a \times 16a$ system is provided in Fig. 8(a)–(d). In the pure system, vibrations are the primary source of atomic displacements in perfect crystals as the temperature rises to T_m [28]. The system starts to vibrate thermally as the temperature gradually increases and some atoms begin to diffuse. Atoms jump from their equilibrium sites to adjacent positions, and those involved in diffusion make a significant contribution to MSD [9,26]. Fig. 8(a) shows that the MSD values are

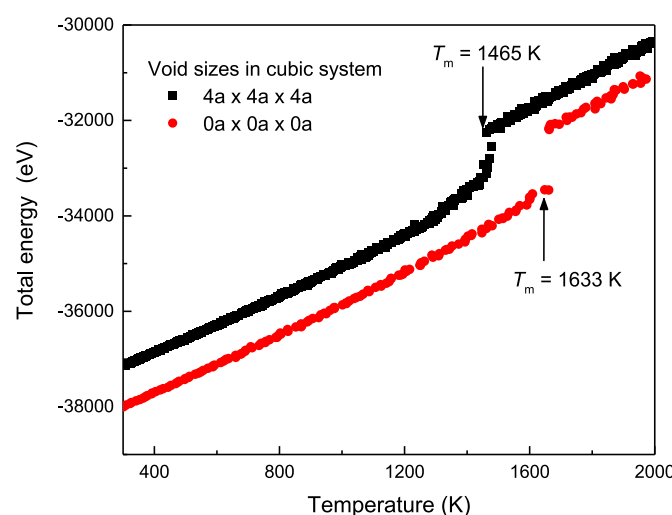


Fig. 6. Variation of the total energy with temperature during the melting of the removed a cubic defect of $4a \times 4a \times 4a$ and $0a \times 0a \times 0a$ (a perfect crystal) is given in the $14a \times 14a \times 14a$.

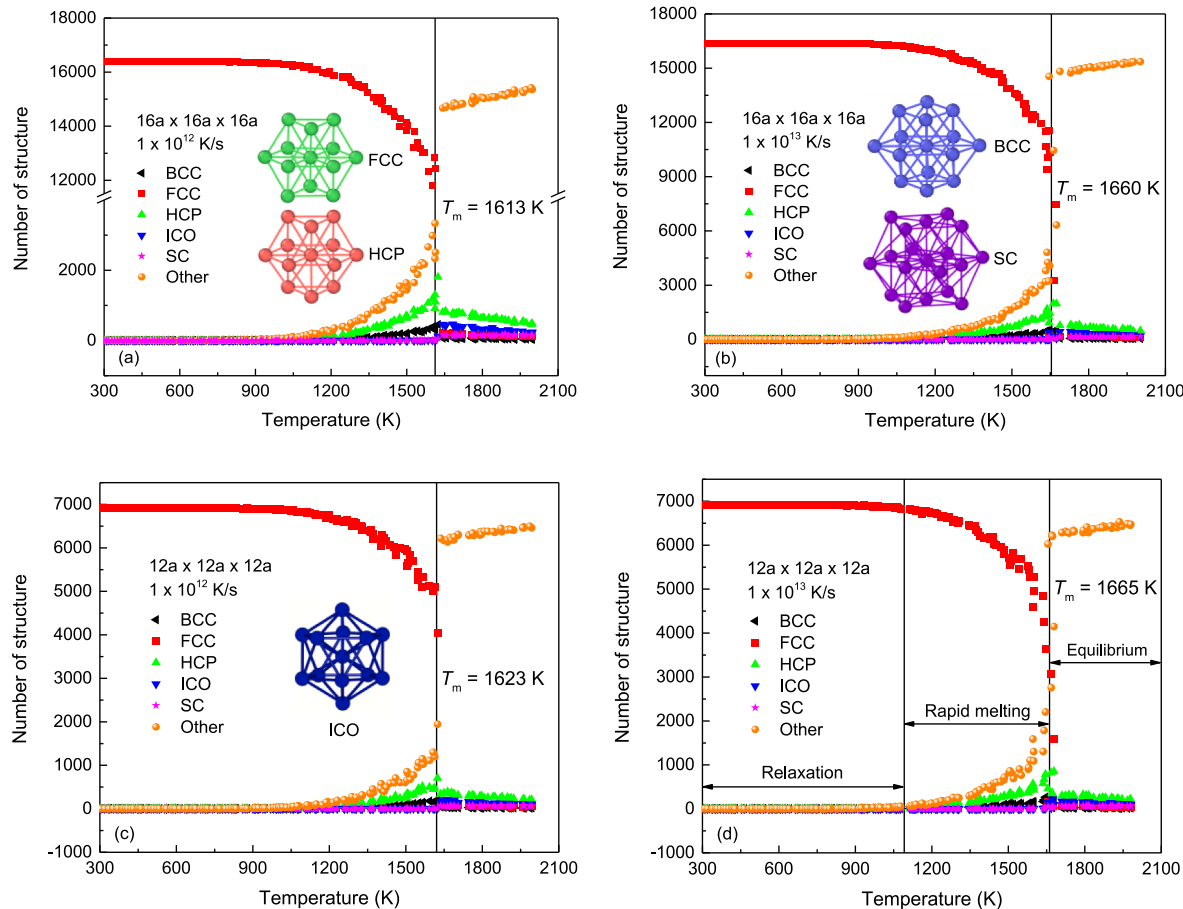


Fig. 7. Temperature dependence of the number of atomic structures, including FCC, HCP, BCC, SC, ICO, and Other clusters, for the $16a \times 16a \times 16a$ and $12a \times 12a$ at the heating rates of 1×10^{12} K/s and 1×10^{13} K/s obtained using the polyhedral template matching method, where (a) $16a \times 16a \times 16a$ and 1×10^{12} K/s, (b) $16a \times 16a \times 16a$ and 1×10^{13} K/s, (c) $12a \times 12a \times 12a$ and 1×10^{12} K/s, and (d) $12a \times 12a \times 12a$ and 1×10^{13} K/s.

small for the temperature range of 1000–1600 K, with the system fluctuating around a certain equilibrium value over time. This indicates that the system is in the solid state and the atoms undergo thermal vibration at equilibrium. However, there is a tendency for the MSD to increase with temperature, signifying stronger thermal motion at higher temperatures, in line with theoretical analysis [9,13,26]. Fig. 8(c) and its corresponding D. demonstrate that the system lacks movement behavior. Fig. 8(b) reveals that the MSD between 1610 K and 1620 K appears slightly larger compared to Fig. 8(a), and the values increase slowly with time, indicating partial melting, i.e., pre-melting, has occurred. The lattice structure is disrupted and atoms are removed from their equilibrium positions. Although the MSD at 1610 K increases linearly, the system lacks the mobility of a liquid as evidenced by the tiny slope, and is in an accelerated energy storage phase, as shown in D in Fig. 8(c). The evolution of the atomic structure at 1610 K and 1620 K, determined by the PTMM method, reveals that the FCC comprises about 57.5% at 1610 K, with the Other clusters and HCP occupying 30.7% and 10.3%, respectively, and BCC, SC, and ICO about 1.5%. At 1620 K, the occupancy of Other clusters is about 91%, indicating extensive melting. The Other cluster increases, and the FCC decreases with increasing relaxation, in accordance with the typical features of a liquid [40]. However, the MSD values of the system increase rapidly with time between 1620 K and 2100 K, suggesting that the system has melted completely. Finally, it is possible to determine from the MSD and D that the T_m for the $16a \times 16a \times 16a$ falls between 1610 K and 1620 K, consistent with the previous results in the present study. From the MSD slope of 1620 K, the corresponding D can be estimated to be $5.14 \times 10^{-9} \text{ m}^2/\text{s}$, which is consistent with the existing result of $5.2 \times 10^{-9} \text{ m}^2/\text{s}$ at

1620 K [41]. This is also supported by atomic structure analysis. The T_m for the $16a \times 16a \times 16a$ system is higher than the experimental result of 1357 K [35], and deviations from the experimental T_m are common [9, 21,31]. The experimental T_m for Cu is reported as 1357 K [35]. However, various simulation methods yield different results, contributing to the disagreement in reported values. The hysteresis method provides results of 1295 K, 1284 K, 1273 K, and 1239 K [21], the two-phase method gives values of 1324 K and 1323 K [21], the interface pinning method yields results of 1315 K [21], the nonequilibrium thermodynamic integration method reports values of 1316 K [21], modified void method produces results of 1327 K [21], and the modified Z method presents values of 1321 K [22]. This discrepancy is observed not only in Cu but also in other metals and compounds such as Al [42], ZnO [43], CaO [9,13], and CaF₂ [44]. From the perspective of MD simulation methods, the limited number of atoms in the simulated system and the imposition of three-dimensional periodic boundary conditions contribute to the observed discrepancies. Additionally, the accuracy and precision of simulation results are influenced by the potentials used to describe interatomic interactions, which often have their basis in empirical or semi-empirical methods. Regarding the methods applied to calculate the melting temperature, single-phase methods exhibit a notable degree of superheating, as seen in the hysteresis method and the Z method. In contrast, results obtained based on the solid–liquid coexistence method are considered more reliable and tend to be closer to experimental values [21].

Additionally, in a system of $16a \times 16a \times 16a$ with a heating rate of 1×10^{12} K/s, the RDF in the range of 1000–1800 K is displayed in Fig. 9. All twelve RDFs exhibit a distinct first peak, indicating the presence of a

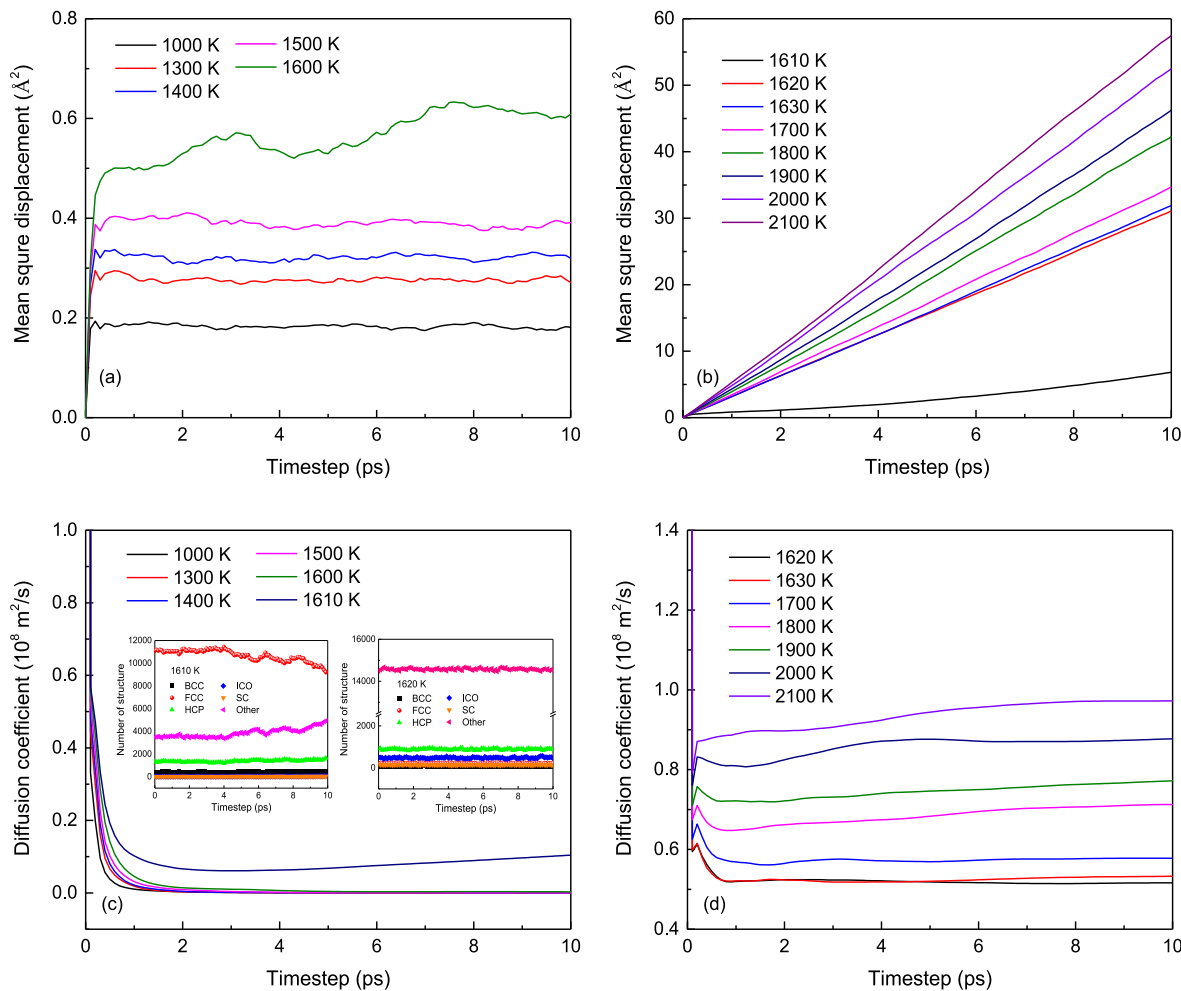


Fig. 8. Mean square displacements (a) and (b) versus diffusion coefficients (c) and (d) for the system obtained from the atomic trajectories with temperature at $16a \times 16a \times 16a$ and a heating rate of $1 \times 10^{12} \text{ K/s}$: (a) 1000–1600 K, (b) 1610–2100 K, (c) 1000–1610 K, and (d) 1620–2100 K. The interpolation shows the evolution of the atomic structure at 1610 K and 1620 K, respectively.

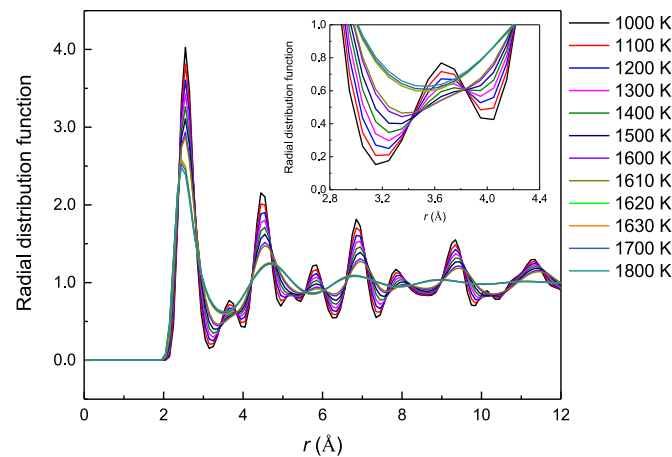


Fig. 9. Evolution of the radial distribution function of the system with temperature for $16a \times 16a \times 16a$ system at a heating rate of $1 \times 10^{12} \text{ K/s}$.

strongly short-range ordered structure. The first peak of the RDF decreases slightly in intensity as the temperature continues to elevate, and the subsequent peaks gradually decrease. Comparing the RDFs at 1610 K and 1620 K, it is evident that the subsequent peaks at 1620 K decrease and even smooth out. This reveals that the orderliness of the atoms

weakens during the heating process, signifying that the heating intensifies their thermal vibrations. The second peak of the RDF curves starts to disappear when the temperature reaches 1620 K, indicating that the system has melted intensively, exhibiting the characteristics of a liquid. This observation aligns with the analysis results of MSD and D .

4. Conclusions

In this work, we have conducted a comprehensive investigation of the melting behavior of Cu using MD simulations. The major findings are as follows: (1) Melting involves a structural transition, where the disappearance of the FCC structure rapidly transforms into HCP, ICO, FCC, SC, and Other clusters in the vicinity of pre-melting. This melting behavior remains consistent across different heating rates and atomic numbers. The structural transitions contributed to the superheating of the T_m for Cu, with temperature remaining the primary factor influencing atomic structure distribution. (2) Analysis MSD, D , and RDF reveals that, after melting, the crystals exist in a liquid state for a certain duration, characterized by limited vibrational amplitude of the atoms. As the temperature continues to rise, the atoms in the liquid exhibit substantial movement, leading to complete melting of the system. (3) Surface melting involves inhomogeneous nucleation from both the outside and inside, while bulk melting is associated with homogeneous nucleation. The temperature of bulk melting is higher than that of surface melting, and pre-melting is observed in both processes. Anisotropy is evident in surface melting, where higher surface energy corresponds

to lower T_m . (4) Simulation results for different orientations show generally consistent T_m values along the [100], [110], and [111] directions, indicating a lack of significant anisotropy along these orientations. (5) The formation and growth of the liquid phase are driven by high heating rates or the movement of atoms around defects, contributing to the lower the temperature of inhomogeneous nucleation melting compared to homogeneous nucleation.

CRediT authorship contribution statement

Xinwei Wang: Conceptualization, Formal analysis, Investigation, Methodology, Software, Writing – original draft, Writing – review & editing. **Mengxin Yang:** Formal analysis, Investigation, Software. **Bohan Cao:** Conceptualization, Data curation, Methodology. **Xiaoqian Gai:** Investigation, Methodology, Writing – review & editing. **Yibo Sun:** Conceptualization, Methodology, Software. **Fubo Tian:** Funding acquisition, Project administration, Supervision, Validation, Writing – review & editing. **Liang Li:** Data curation, Formal analysis, Supervision, Visualization, Writing – original draft, Writing – review & editing.

Declaration of competing interest

We declare that there is no conflict of interest in the manuscript submitted and that it is published with the consent of all authors. I would like to declare on behalf of my co-authors that the work described was original research that has not been published previously, and not under consideration for publication elsewhere, in whole or in part. All the authors listed have reviewed the revised manuscript and approved to submit to your journal.

Data availability

No data was used for the research described in the article.

Acknowledgements

This work was supported by the National Natural Science Foundation of China (Nos. 11574109 and 91745203), parts of calculations were performed in the High-Performance Computing Center (HPCC) of Jilin University.

References

- [1] K. Sunil, M.P. Singh, B.S. Sharma, Comput. Condens. Matt. 35 (2023) e00813.

- [2] R.G. Kraus, J.P. Davis, C.T. Seagle, D.E. Fratanduono, D.C. Swift, J.L. Brown, J. H. Eggert, Phys. Rev. B 93 (2016) 134105.
- [3] M.N. Magomedov, Vacuum 213 (2023) 112079.
- [4] T.D. Cuong, A.D. Phan, Vacuum 185 (2021) 110001.
- [5] A.B. Belonoshko, J. Fu, G. Smirnov, Phys. Rev. B 104 (2021) 104103.
- [6] N.V. Nghia, H.K. Hieu, Chem. Phys. 553 (2022) 111389.
- [7] M.N. Magomedov, Comput. Condens. Matt. 31 (2022) e00673.
- [8] D. Ashwini, V.S. Sharma, K. Sunil, Eur. Phys. J. Plus 137 (2022) 545.
- [9] X.-W. Wang, X.-W. Sun, T. Song, J.-H. Tian, Z.-J. Liu, Vacuum 209 (2023) 111717.
- [10] N.V. Kozyrev, Int. J. Thermophys. 44 (2023) 31.
- [11] S. Safalutin, S. Gürmen, Comput. Mater. Sci. 183 (2020) 109842.
- [12] T. Begasheva, T. Falyakhov, S. Petukhov, M. Sheindlin, A. Vasin, P. Vervikishko, J. Am. Ceram. Soc. 104 (2021) 3461–3477.
- [13] C.M. Alvares, G. Deffrennes, A. Pisch, N. Jakse, J. Chem. Phys. 152 (2020) 084503.
- [14] F.A. Lindemann, Phys. Z. 11 (1910) 609–614.
- [15] T. Ninomiya, J. Phys. Soc. Jpn. 44 (1978) 263–268.
- [16] E.A. Kraut, G.C. Kennedy, Phys. Rev. 151 (1966) 668.
- [17] M. Born, J. Chem. Phys. 7 (1939) 591.
- [18] X. Fan, X. Chen, D. Pan, Y. Liu, P. Liu, M. Li, Phys. Rev. B 104 (2021) 134204.
- [19] K. Li, R. Khanna, J. Zhang, G. Li, H. Li, C. Jiang, M. Sun, Z. Wang, Y. Bu, M. Bouhadja, Z. Liu, M. Barati, J. Mol. Liq. 290 (2019) 111204.
- [20] N. Joshi, N. Mathur, T. Mane, D. Sundaram, Comput. Mater. Sci. 145 (2018) 140–153.
- [21] Y. Zou, S. Xiang, C. Dai, Comput. Mater. Sci. 171 (2020) 109156.
- [22] S. Wang, G. Zhang, H. Liu, H. Song, J. Chem. Phys. 138 (2013) 134101.
- [23] D. Alfe, C. Cazorla, M.J. Gillan, J. Chem. Phys. 135 (2011) 024102.
- [24] M.P. Hazarika, S.N. Chakraborty, Chem. Phys. Lett. 730 (2019) 521–526.
- [25] Y. Zhang, E.J. Maginn, J. Chem. Phys. 136 (2012) 144116.
- [26] G. Zhang, X. Fan, Q. Zhang, Q. Li, Y. Wu, M. Li, Acta Mater. 239 (2022) 118281.
- [27] X. Fan, D. Pan, M. Li, Acta Mater. 193 (2020) 280–290.
- [28] X. Fan, D. Pan, M. Li, J. Phys.: Condens. Matter. 31 (2019) 095402.
- [29] M.M. Vopson, N. Rogers, I. Hepburn, Solid State Commun 318 (2020) 113977.
- [30] S.A. Khrapak, Phys. Rev. Res. 2 (2020) 103020.
- [31] J. Jiang, X. Zhang, F. Ma, S. Dong, W. Yang, M. Wu, Chem. Phys. Lett. 763 (2021) 138187.
- [32] S. Plimpton, J. Comput. Phys. 117 (1995) 1–19.
- [33] Y. Mishin, M. Mehl, D. Papaconstantopoulos, A. Voter, J. Kress, Phys. Rev. B 63 (2001) 224106.
- [34] P.M. Larsen, S. Schmidt, J. Schiøtz, Model. Simul. Mater. Sci. Eng. 24 (2016) 055007.
- [35] T. Karabacak, J.S. DeLuca, P.-I. Wang, G.A. Ten Eyck, D. Ye, G.-C. Wang, T.-M. Lu, J. Appl. Phys. 99 (2006) 064304.
- [36] M. Fishman, H.L. Zhuang, K. Mathew, W. Dirschka, R.G. Hennig, Phys. Rev. B 87 (2013) 245402.
- [37] Y. Han, K.C. Lai, A. Lii-Rosales, M.C. Tringides, J.W. Evans, P.A. Thiel, Surf. Sci. 685 (2019) 48–58.
- [38] A. Stukowski, Model. Simul. Mater. Sci. Eng. 18 (2009) 015012.
- [39] Y. Gao, T. Gao, L. Li, Q. Xie, Q. Chen, Z. Tian, Y. Liang, B. Wang, Vacuum 194 (2021) 110525.
- [40] O. Roik, O. Samsonnikov, V. Kazimirov, V. Sokolskii, S. Galushko, J. Mol. Liq. 151 (2010) 42–49.
- [41] A. Meyer, Phys. Rev. B 81 (2010) 012102.
- [42] A.V. Karavaev, V.V. Dremov, T.A. Pravishkina, Comput. Mater. Sci. 124 (2016) 335–343.
- [43] X.-W. Wang, X.-W. Sun, T. Song, J.-H. Tian, Z.-J. Liu, Appl. Phys. A 128 (2022) 482.
- [44] C. Cazorla, D. Errandonea, J. Phys. Chem. C 117 (2013) 11292–11301.